Routing Edge States in an Anisotropic Elastic Topological Insulator

Shuowei An,[1] Tuo Liu,[2] Yafeng Chen,[1,3,*] Li Cheng,[1,†] and Jie Zhu[4,‡]

[1] *Department of Mechanical Engineering, Hong Kong Polytechnic University, Hong Kong, China*
[2] *Key Laboratory of Noise and Vibration Research, Institute of Acoustics, Chinese Academy of Sciences, Beijing 100190, China*
[3] *State Key Laboratory of Advanced Design and Manufacturing for Vehicle Body, Hunan University, Changsha 410082, China*
[4] *Institute of Acoustics, School of Physics Science and Engineering, Tongji University, Shanghai 200092, China*

(Received 18 August 2022; revised 4 October 2022; accepted 11 October 2022; published 22 November 2022)

Topological insulators, protected by nontrivial band topology, exhibit backscattering-immune edge states, conducive to robust waveguiding with high efficiency. However, routing such robust edge states has been restricted by the isotropy in conventional unit cells respecting crystalline symmetries, such as C_{4v} symmetry in a square lattice or C_3 symmetry in a hexagonal lattice. We effectively tackle this issue by introducing anisotropic coupling into a square lattice. With theoretical prediction from the discrete mechanical model, we experimentally demonstrate that such anisotropy can enable distinctive topological phases along different directions, giving rise to directional edge states. In addition, when the bands along the two directions are topologically identical and untrivial, the coexisting edge states have distinctive frequency ranges, giving rise to the frequency-routed properties. Our work offers an effective strategy for the robust steering, filtering, detection, and transmission of elastic waves through tactical edge state routing.

DOI: 10.1103/PhysRevApplied.18.054071

I. INTRODUCTION

Elastic wave manipulation is a thriving topic due to the exciting wave phenomena it enables and the great potential it offers for numerous applications, such as vibration control [1,2], structural health monitoring [3,4], and noninvasive disease treatment [5]. Recently, inspired by the emerging band-topology theory in condensed matter physics, topological insulators (TIs) in elastic or acoustic media have been implemented in phononic crystals (PCs) [6–10], referred to as phononic topological insulators (PTIs). To date, several types of PTIs have been developed based on various physical mechanisms like the quantum Hall effect [9,11,12], the quantum spin Hall effect [10,13,14], or the quantum valley Hall effect [15–19]. These PTIs all feature topologically protected edge states that are impervious to contaminants and have unquestionably significant potential in high-efficiency waveguiding and communication. However, routing such robust edge states is challenging because all domain walls in the PTIs host topological edge states with the same frequency range. One type of approach is to "move" the domain wall itself by altering the topological phase of specific regions. In an elastic wave system, such a strategy could be implemented by physically adjusting the mass [20], stiffness [21], or orientation angle of scatterers [22]. Although external active controls, such as the arrangement of programmable magnet lifting [20] or piezoelectric shunting circuits [21], can endow their reconfigurabilities to certain extent, the resultant bulky attachment parts and complicated design are undesirable for practical applications. The alternative option is to construct domain walls by assembling topological insulators that support edge states with different frequency ranges while sharing a common bulk band gap [23,24]. The idea has been conceptionally proposed in photonic systems, but experimental realization is still lacking because of the stringent requirement on sample-machining precision. A similar problem applies to techniques based on multibranch band gaps in acoustic and elastic wave systems [25–27], which are vulnerable to slight dimensional changes. In summary, the demand for a practical scheme for edge-state routing is imminent.

Meanwhile, anisotropy is shown to enable unique properties in metamaterials, such as fluidlike elasticity [28], deep-subwavelength imaging [29], wave routing [30,31], and perfect mode conversion [32]. Intentionally created anisotropy also offers an option to resolve the aforementioned problem of wave routing in TIs, thanks to its inherent directionality. Conventional TIs are made up of isotropic unit cells that adhere to certain spatial symmetries, such as C_{4v} symmetry in a square lattice, imposing identical topological properties along

*yfchen@hnu.edu.cn
†li.cheng@polyu.edu.hk
‡jiezhu@tongji.edu.cn

two orthogonal directions. Such a restriction could be lifted by introducing anisotropic coupling, leading to zero-dimensional topologically localized states rooted in nonzero-edge dipolar polarization [33] or nontrivial dislocation [34] in photonics. In particular, this could also entail directional edge states in an acoustic quantum Hall TI [35], providing a promising solution for wave routing. The proposed quantum Hall TI requires the breaking of time-reversal symmetry, which is challenging to achieve experimentally in elastic [9] or acoustic systems [36] and detrimental to the practical implementation of such a scheme. Meanwhile, thorough theoretical investigations of the topological transition in an anisotropic TI in elastic systems are still lacking, and the properties of potentially occurring anisotropic edge states remain unexplored.

To tackle these challenges, this study proposes an anisotropic elastic TI realized in a pillared plate featuring directional and frequency-routed edge states. We start with a mechanical lattice model in Sec. II and compare the band structure of the proposed design with anisotropic unit cells to that of the conventional isotropic design. It is found that the anisotropy, created by adjusting the ratio of intra- and interstiffnesses along different directions, could shape the band structure and tailor the topological phases directionally and independently. When the topological phases along the two directions are tweaked to be different, the edge states become directional. Meanwhile, even if nontrivial topological phases are equal, the edge states along the two directions could have distinct frequency ranges, which can be exploited for frequency routing. There are three possible routing schemes, which are switchable based on the operating frequency. In Sec. III, PCs are designed and constructed based on the discrete model to further confirm the properties of edge states numerically and experimentally. Finally, Sec. IV concludes with our findings.

II. THEORY: MECHANICAL LATTICE MODEL

We establish an anisotropic mechanical lattice model to discuss the topological properties of a square lattice. In contrast to the conventional isotropic case, the band structures and topological phases of the anisotropic ones may be modified directionally and independently by tuning the coupling strength. As a result, four different types of two-dimensional (2D) topological phases can be realized in the anisotropic unit cells. Following an investigation of the unusual band structures, we further study the edge states in ribbon structures and discuss their properties, including directionality and frequency routing.

A. Band structures and topological property

The top of Fig. 1(a) shows a schematic of a conventional unit cell with a square lattice. The four masses, m (circles filled in gray), are intraconnected by springs with stiffness, K_{intra}, and interconnected by springs with stiffness K_{inter}. Such an isotropic unit cell respects C_{4v} symmetry. The proposed anisotropic unit cell, on the other hand, has different intra- (K^x_{intra}, K^y_{intra}) or interstiffnesses (K^x_{inter}, K^y_{inter}) along the x and y directions. As shown in the bottom of Fig. 1(a),

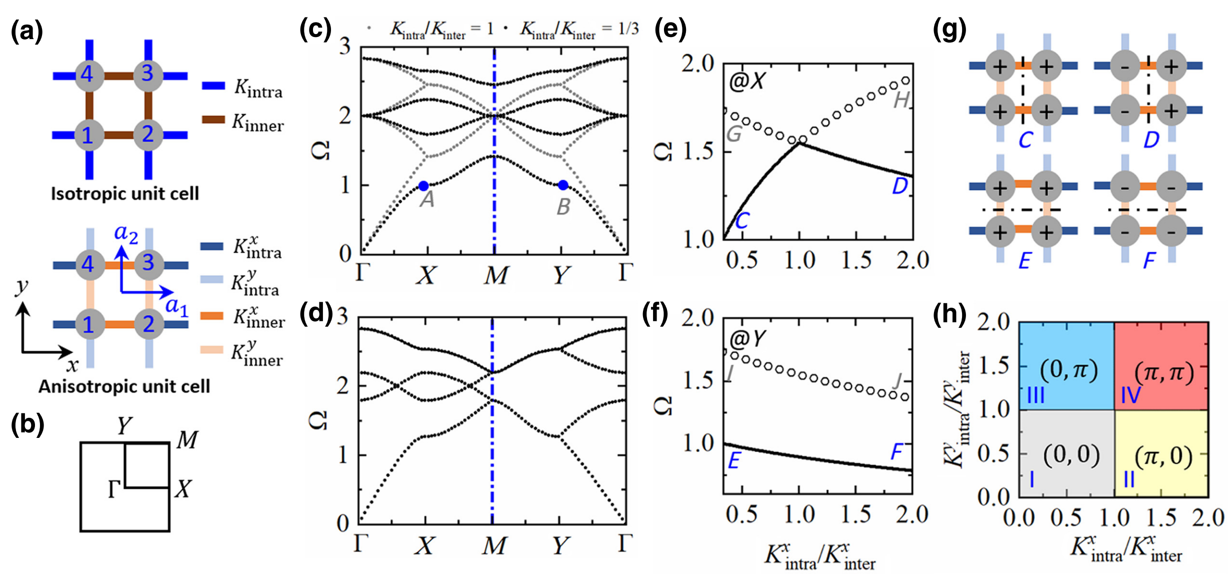

FIG. 1. Band structures of the mechanical lattice models and associated topological phase transition. (a) Schematic illustration of discrete mechanical models involving isotropic (top) and anisotropic (bottom) unit cells. (b) First Brillouin zone of the unit cell. Band structures of (c) isotropic and (d) anisotropic cases. Evolution of the two lowest bands at (e) X and (f) Y points with respect to $K^x_{\mathrm{intra}}/K^x_{\mathrm{inter}}$. (g) Phases of eigenstates at A–D marked in (e),(f). Signs + and − represent phases 0 and π, respectively. (h) Classification of anisotropic unit cells based on distinctive 2D polarization.

it instead respects C_{2v} symmetry, and the first Brillouin zone (BZ) is presented in Fig. 1(b).

We obtain the mechanical lattice's governing equation and cast the calculation of the corresponding band structure into an eigenvalue problem (see the detailed formula in Appendix A) [15]. The topological properties can be determined by the 2D polarization $P = (P_x, P_y)$, which is defined by [37,38]

$$P_i = \pi\left(\sum_n q_i^n \text{modulo } 2\right), \quad (-1)^{q_i^n} = \frac{\eta_n(A_i)}{\eta_n(\Gamma)}, \qquad (1)$$

where $i = x, y$ denotes the direction. η_n denotes the parity at the high-symmetry points (X, Y, and Γ) for the nth band. It can be determined by the symmetry of the eigenstate profiles [the mirror symmetric one corresponds to even parity (+), while the antisymmetric one corresponds to odd parity (−)]. It should be noted that, at the static limit, the parity at Γ is always even due to its mirror symmetric profile. The summation over n denotes all bands below the band gap, which is set to one to consider the lowest band gap throughout this paper. According to Eq. (1), P_x is determined to be 0 (π) when the eigenstate at X is mirror symmetric (mirror antisymmetric). Similarly, P_y can also be determined by the eigenstate at Y.

We first examine a typical lattice made up of isotropic unit cells by setting $K_{\text{intra}} = K^x_{\text{intra}} = K^y_{\text{intra}}$ and $K_{\text{inter}} = K^x_{\text{inter}} = K^y_{\text{inter}}$. When the ratio of $K_{\text{intra}}/K_{\text{inter}}$ is detuned into three regimes, i.e., less than 1, equal to 1, and greater than 1, the band gaps along both $\Gamma - X$ and $\Gamma - Y$ directions simultaneously open, close, and reopen, accompanied by the topological transformation from trivial to nontrivial. The band structures of the models are exemplified using $K_{\text{intra}} = K_{\text{inter}} = 1$ N/m, $K_{\text{intra}} = 1/3$(N/m), and $K_{\text{inter}} = 1$ N/m ($m = 1$ kg in this paper, unless otherwise stated) in Fig. 1(c). Restricted by C_{4v} symmetry, i.e., isotropic stiffnesses in the unit cell, the bands along the two directions are identical, and the whole band-structure curves are always symmetric about the high-symmetric point, M. More importantly, the topological invariants along both directions must be the same. We take the case of $K_{\text{intra}} = 1/3$(N/m) and $K_{\text{inter}} = 1$ N/m as an example and calculate its 2D polarization, P, according to Eq. (1). As expected, the resultant P is (0, 0) after considering the same parities of eigenstates at the high-symmetry points marked by A and B in Fig. 1(c) (see the eigenstates in Fig. 8 in Appendix B), satisfying $P_x = P_y$.

In comparison, such a constraint can be lifted by introducing anisotropic coupling. Setting different intra- and interstiffnesses for the two directions, namely, $K^x_{\text{intra}} = 1/3$(N/m), $K^x_{\text{inter}} = 1$ N/m, $K^y_{\text{intra}} = 1$ N/m, and $K^y_{\text{inter}} = 1$ N/m, the band structures become asymmetric along M. As shown in Fig. 1(d), a band gap opens along the $\Gamma - X$ direction but closes along the $\Gamma - Y$ direction. Moreover, when $K^x_{\text{intra}}/K^x_{\text{inter}}$ changes from 1/3 to 2, while $K^y_{\text{intra}}/K^y_{\text{inter}}$ remains 1/3, the band gap along the $\Gamma - X$ direction first closes (when $K^x_{\text{intra}}/K^x_{\text{inter}}$ increases to 1) and then reopens, as seen in Fig. 1(e). During this process, parity at the X point flips from even to odd [see the top of Fig. 1(g)], and the polarization, P_x, flips from 0 to π. In contrast, the band gap along the $\Gamma - Y$ direction remains open, and parity at the Y point is always even [see the bottom of Fig. 1(g)], indicating P_y remains zero with no topological phase transition occurring. Therefore, the adjustable intra- and interstiffness ratios along the two directions allow us to independently and directionally shape the band structure while controlling the topological phases. Furthermore, the eigenstates at specific points in the two bands near the band gap, marked in Figs. 1(e) and 1(f), show opposite parities (eigenstates at G–J are given in Fig. 8 in Appendix B).

Based on different 2D polarization values, the anisotropic lattices can be categorized into four types in the parameter space spanned by the ratios $K^x_{\text{intra}}/K^x_{\text{inter}}$ and $K^y_{\text{intra}}/K^y_{\text{inter}}$, as seen in Fig. 1(h). For example, in region III, where $K^x_{\text{intra}}/K^x_{\text{inter}} < 1$ while $K^x_{\text{intra}}/K^x_{\text{inter}} > 1$, the band is topologically trivial along the x direction while nontrivial along the y direction. Such a category provides a clear guideline for securing the desired topological phases in parameter space.

B. Edge states

The bulk-boundary correspondence principle ensures that topologically protected edge states exist along the domain wall between two structures with distinctive topological phases. To study the edge states in anisotropic topological insulators, three types of ribbon mechanical lattices are constructed by stacking 1×8 anisotropic unit cells and 1×8 trivial isotropic unit cells, as illustrated in Figs. 2(a) and 2(b). The one shown in Fig. 2(a) is for edge-state calculations along the x direction, whereas Fig. 2(b) presents the one for the edge-state calculations along the y direction. The lattice comprises eight trivial isotropic unit cells with 2D (0, 0) polarization to provide a reliable physical boundary. The associated derivation for the band dispersion is given in Appendix C.

When the ratios of the stiffnesses of anisotropic unit cells are identical and located in region I in Fig. 1(h), $K^x_{\text{intra}} = 1/3$(N/m), $K^x_{\text{inter}} = 1$N/m, $K^y_{\text{intra}} = 1/3$(N/m), and $K^y_{\text{inter}} = 1$ N/m. For isotropic ones, $K_{\text{intra}} = 1/3$(N/m) and $K_{\text{inter}} = 1$ N/m. Because the 2D polarization of the anisotropic lattice is (0, 0), edge states do not exist along either the x or y directions, which is confirmed by the calculated band dispersion in Fig. 2(c). When anisotropy is introduced by setting $K^x_{\text{intra}} = 1/3$(N/m), $K^x_{\text{inter}} = 1$ N/m , $K^y_{\text{intra}} = 1$ N/m, and $K^y_{\text{inter}} = 1/3$(N/m) [region III in Fig. 1(h)], the topological phases along the two directions diverge, and the 2D polarization becomes (0, π). According to the bulk-boundary correspondence, an edge state will appear along the x direction but not the y direction, as shown in

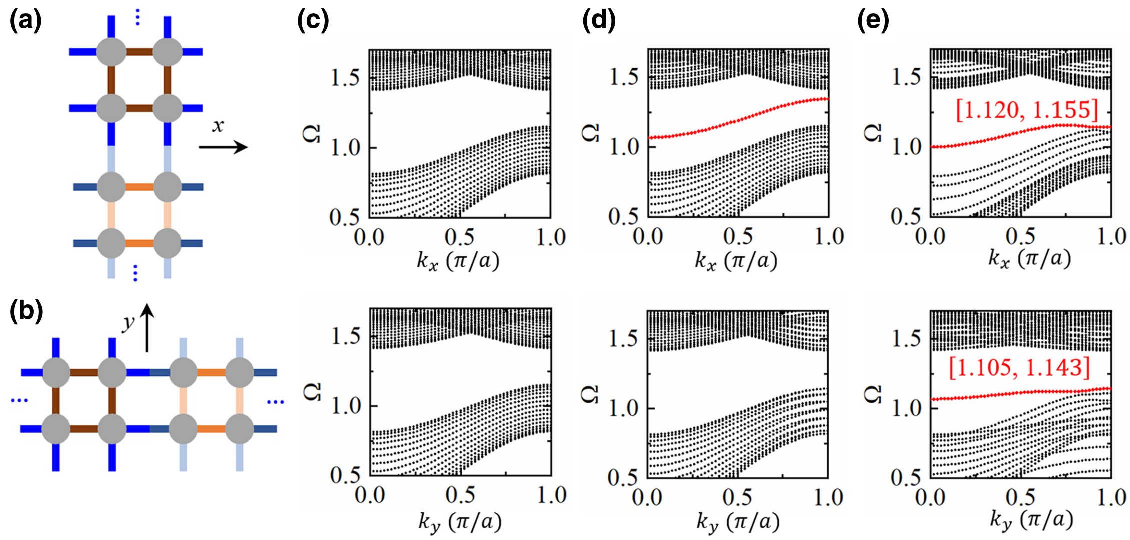

FIG. 2. Band dispersion of ribbon mechanical lattice models. Schematics of the ribbon structure arrayed by eight isotropic and eight anisotropic unit cells to verify the edge states along (a) x and (b) y directions. Band dispersions of ribbon structures with 2D polarizations of their composed anisotropic lattices of (c) (0, 0), (d) (0, π), and (e) (π, π).

Fig. 2(d). Such directional edge states originate from the imposed stiffness anisotropy, which is not present in a conventional isotropic topological insulator.

Aside from directionality, the anisotropy of stiffness can also bridge the propagation directions and the working frequency of the edge states, allowing for frequency routing. Setting $K_{\text{intra}}^x = 1$ N/m, $K_{\text{inter}}^x = 1/3$(N/m), $K_{\text{intra}}^y = 1$ N/m, and $K_{\text{inter}}^y = 1/10$(N/m) [region IV in Fig. 1(h)], the 2D polarization becomes (π, π), indicating nontriviality along both directions. Therefore, the edge states can persist in both directions, as seen in Fig. 2(e). Moreover, although the topological phases along the two directions are identical, the existing frequency ranges for the edge states might differ due to the deliberately established stiffness anisotropy. Figure 2(e) shows a dimensionless frequency range of [1.105, 1.143] for the y direction but [1.120, 1.155] for the x direction. The two frequency ranges overlap and create three regions: [1.105, 1.120], [1.120, 1.143], and [1.143, 1.155]. When the operating frequency is in the first (third) region, the edge state can only transmit along the y (x) direction. While the edge state transmits along both directions when the operating frequency is within the second region. Edge states with different frequencies can therefore be routed along separate directions.

III. SIMULATION AND EXPERIMENTS: ELASTIC PHONONIC CRYSTAL OF PILLARED PLATE

The aforementioned mechanical lattice model is a useful platform for capturing the topological phase transition of the anisotropic unit cells. It predicts that, by modulating the anisotropy of stiffnesses in the square lattice, the edge states of topological insulators can be tuned to deliver desired directionality and frequency routing. Here, we demonstrate how to actualize anisotropic topological properties in a proposed PTI, the pillared elastic plate.

A. Band structures

Figure 3(a) depicts the proposed PC's unit cell. It consists of four identical cuboid steel pillars joined to an aluminum plate and resembles the mechanical lattice model discussed in Sec. II A. Here, the pillars and substrate plate act as concentrated masses and springs, respectively. The lengths and widths of the pillars are equal and denoted by b, while the height is represented by h. The plate thickness and lattice constant are denoted by d and a, respectively. Here, we set $a = 30$ mm, $d = 2.75$ mm, $b = 4$ mm, and $h = 15$ mm. The distances between pillars along the x and y directions, denoted by l_x and l_y, are crucial parameters for adjusting the intra- and interstiffness ratios along the two directions. The Young's modulus (E), Poisson's ratio (ν), and density (ρ) of the aluminum substrate plate (steel pillars) are 6.9×10^{10} Pa, 0.32, and 2900 kg/m^3 (2×10^{11} Pa, 0.3, and 7780 kg/m^3), respectively.

To identify the flexural wave mode, a polarization coefficient, α ($0 \le \alpha \le 1$), is defined as

$$\alpha = \iiint_{\text{unit cell}} |w|^2/(|u|^2 + |v|^2 + |w|^2)dV. \qquad (2)$$

Although other branches, such as symmetric and shear modes, also exist in the band gap of the flexural waves investigated here, they are nearly decoupled from the flexural waves thanks to the low-frequency-thickness

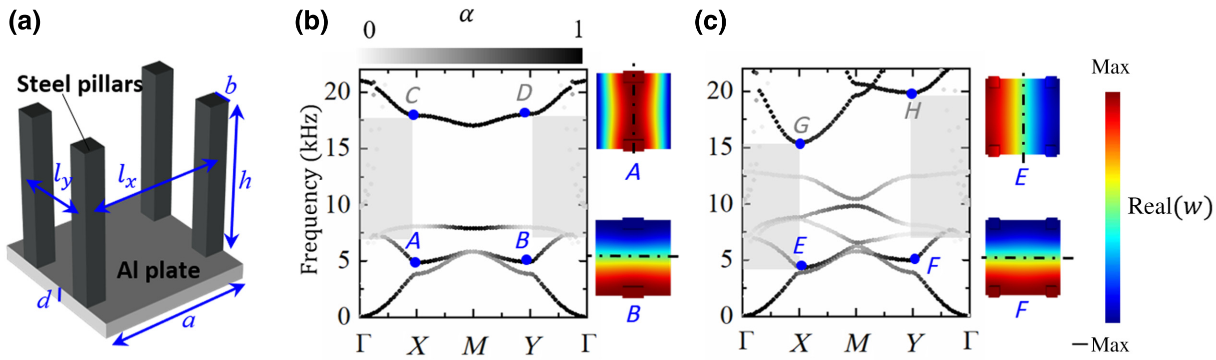

FIG. 3. (a) Unit cell of the proposed PC, comprising an aluminum substrate plate and four attached steel pillars. Band structures of two types of PCs with their 2D polarizations being (b) $(0,\ \pi)$ and (c) $(\pi,\ \pi)$. Gray regions shade the directional band gaps. Insets show the eigenstates of the marked points. Gray (rainbow) color bar represents the value of polarization coefficient α [real part of the out-of-plane displacement, real(w)].

product. We consider two types of anisotropic PCs, type I and II. Their band structures, eigenstates at specific high-symmetry points, and corresponding polarization coefficients are obtained by using the finite-element solver COMSOL and presented in Figs. 3(b) and 3(c).

In the type-I PC, l_x and l_y are set as 4 and 26 mm, respectively, to ensure the intra- and interstiffness ratios are small along the x direction but large enough along the y direction. Figure 3(b) shows the corresponding band structure, with directional band gaps along $\Gamma - X$ and $\Gamma - Y$ sharing the same frequency range of 6.931 to 17.743 kHz. However, the varied parities of eigenstates at the high-symmetry points (designated by A and B) indicate their distinctive topological phases, as seen in the insets of Fig. 3(b). The parity is even at X but odd at Y. As a result, the 2D polarization of type-I PCs is derived as $(0,\ \pi)$, according to Eq. (1).

l_x and l_y are set as 22 and 26 mm in type-II PCs to ensure nontrivial topology along both x and y directions [i.e., 2D polarization is $(\pi,\ \pi)$]. It is confirmed by both odd-parity eigenstate profiles at the high-symmetry points (marked by E and F) of the band below the band gap, as shown in the insets of Fig. 3(c). On the other hand, the frequency ranges of the directional band gaps differ due to the varying intra- and interstiffness ratios along the two directions, as evidenced by the shaded gray areas in the band structure of Fig. 3(c). Such a difference adds to the subsequent frequency-routed edge states.

In addition, the eigenstates at the high-symmetry points of the band above the band gap, labeled as C and D in Fig. 3(b) and G and H in Fig. 3(b), are presented in Fig. 9 in Appendix D to show their opposite parities compared with those below the band gap.

B. Directional edge states

To investigate the topological edge states in type-I PCs, solid ribbon structures (depicted in the left insets of Fig. 4) are constructed from 1×8 trivial isotropic and 1×8 anisotropic unit cells, as described in Sec. II B. According to the bulk-boundary correspondence principle, the edge state of type-I PCs with polarization $(0,\ \pi)$ is ensured along the x direction but disallowed along the y direction. The calculated band dispersions in Fig. 4 confirm

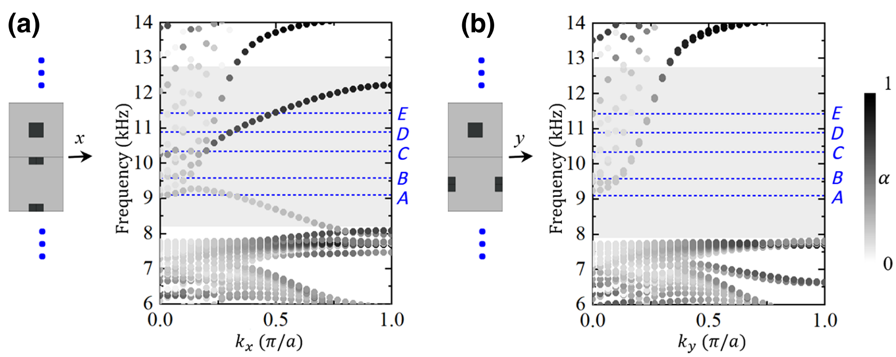

FIG. 4. Band dispersions of solid ribbon structures arrayed by eight isotropic and eight anisotropic unit cells to investigate the edge states in a type-I PC along (a) x and (b) y directions. Left insets of (a),(b) illustrate their respective configurations. Gray-color bar represents the value of polarization coefficient α. A–E are five selected frequencies within the bulk band gap (gray shaded region).

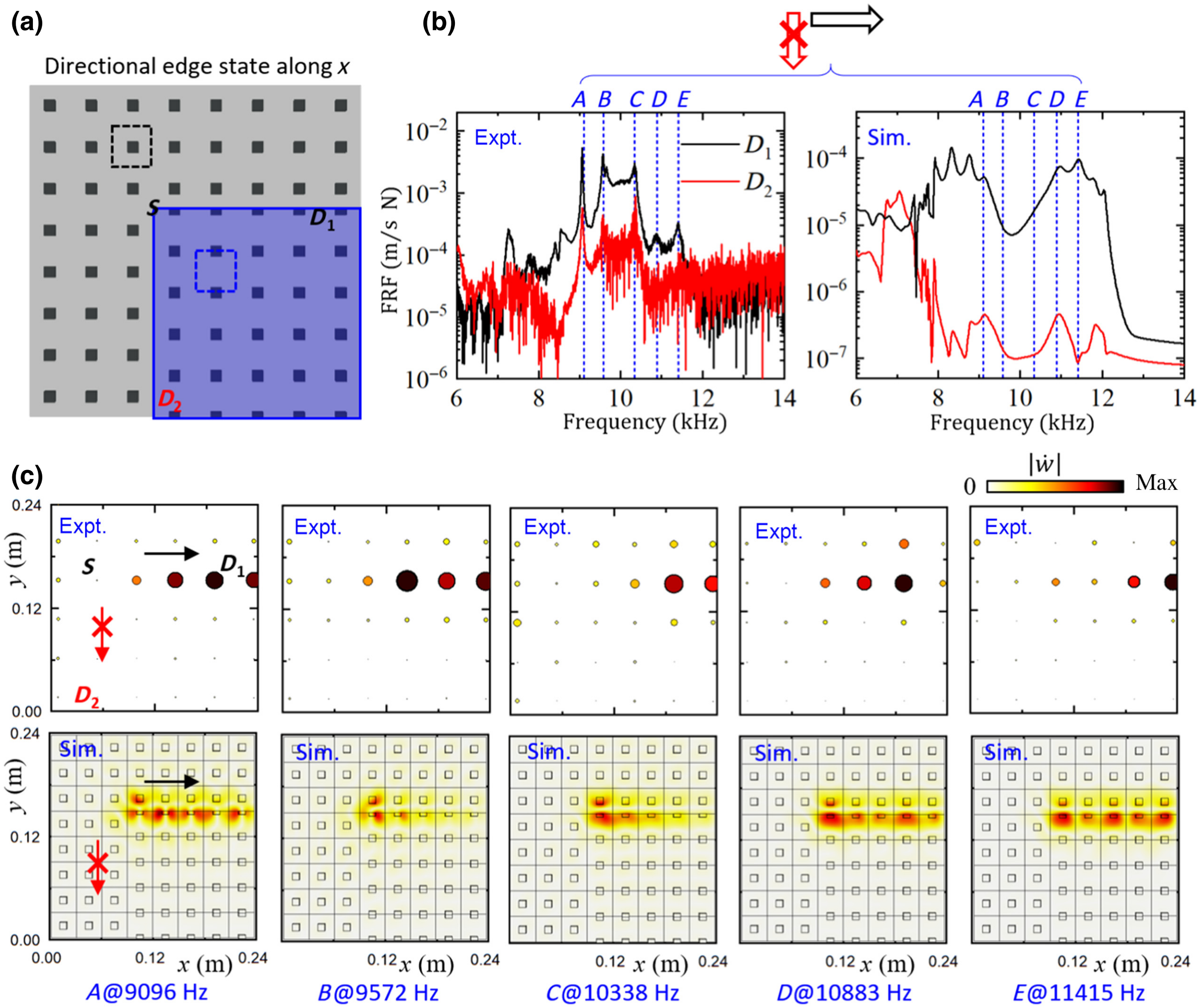

FIG. 5. Validation of the directional edge states. (a) Structure I is composed of isotropic (black dashed frame) and anisotropic (blue dashed frame) unit cells, with 2D polarizations of (0, 0) and (0, π), respectively. S, D_1, and D_2 represent the excitation position and two detecting points, respectively. (b) Measured (left) and simulated (right) frequency-response functions of the structure at D_1 and D_2. (c) Measured (top) and simulated (bottom) fields of FRF corresponding to the selected frequencies A–E marked in (b) and Fig. 4. Both color and radius of the circle reflect the amplitude of FRF at the scanned points.

such directionality, with edge states occurring only (successive in the frequency range from 8.196 to 12.265 kHz) within the band gap along the x direction but not along the y direction.

The directional edge state is further experimentally confirmed in a proposed elastic PTI [shown in Fig. 5(a)], named structure I. It consists of a 5×5 type-I PC surrounded by three layers of trivial isotropic unit cells, followed by the formation of two domain walls along the x and y axes. The excitation source, denoted by S in Fig. 5(a), is positioned at the intersection of the two domain walls to activate any possible edge states. Two detecting points, D_1 and D_2, are used to capture the transmitted wave along the x and y directions, respectively. Experimental details, including sample fabrication, excitation, signal detection, and experimental setup, are given in Appendix E. The left part of Fig. 5(b) presents the measured frequency-response functions (FRFs) along the two directions, which are the complex quantities obtained by dividing the velocity at the detecting point by the force at the source. They reveal that the wave exclusively propagates along the x direction rather than the y direction, with frequencies ranging from 8.1 to 11.5 kHz. The scanned fields at five selected frequencies, marked by A–E, also demonstrate the directionality of such edge states, as seen in the top of Fig. 5(c). As a comparison, the corresponding simulation results are shown in the right part of Fig. 5(b) and the bottom of Fig. 5(c). They are in good agreement with the measured ones, although some peaks exist in the measured FRF, which may come from the imperfect absorption of Blu Tack attached around the samples and potential defective adhesions of pillars. The

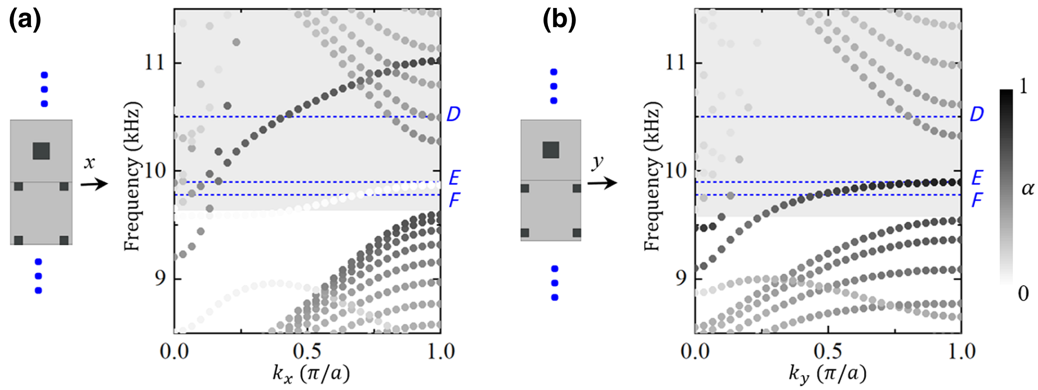

FIG. 6. Band dispersions of the solid ribbon structure arrayed by eight isotropic and eight anisotropic unit cells with 2D polarization of (π, π) to investigate the edge states in the type-II PC along (a) x and (b) y directions. Left insets of (a),(b) illustrate their respective configurations. Gray-color bar represents the value of polarization coefficient α. *D*–*F* are three selected frequencies within the bulk band gap (gray shaded region).

inaccurate material-parameter estimations could also lead to the deviation of the frequency ranges. The simulation settings are detailed in Appendix F.

C. Frequency-routed edge state

A different ribbon structure is built to explore the features of existing edge states in type-II PCs. It is now prepared by stacking 1×8 anisotropic unit cells and 1×8 trivial isotropic unit cells. Because of the anisotropic unit cell's nontrivial 2D polarization (π, π), the edge states should coexist along both directions. This is confirmed by the band dispersions in Figs. 6(a) and 6(b) for the x and y directions, respectively. Remarkably, the two edge states have distinctive band ranges (9.850–11.030 kHz for the x direction and 9.579–9.940 kHz for the y direction), bridging the directions with the working frequencies, allowing for frequency routing. The two interlacing bands, in particular, equip the proposed anisotropic topological insulators with three modes: wave transport along the x direction only, along the y direction only, or along both directions simultaneously. One of the three can be triggered by simply switching the working frequency to the relevant bands.

We test the aforementioned results experimentally for structure II, which comprises a 5×5 type-II PC surrounded by three layers of trivial isotropic unit cells, as shown in Fig. 7(a). As shown in the left part of Fig. 7(b), substantial transmission is observed along both x and y directions, with band ranges of 9.706–10.939 and 8.905–10.094 kHz, respectively, validating the two existing edge states. At the same time, the above two interlacing bands of the edge states also give us three frequency ranges, 8.905–9.706, 10.094–10.939, and 9.706–10.094 kHz, derived from the three patterns corresponding to transport along y or x and both x and y directions of the edge states. The measured fields at the three selected frequencies [marked as *A*–*C* in Fig. 7(b)] support the three patterns, as seen in the top parts of Figs. 7(c)–7(e). Meanwhile, the simulation results also confirm the aforementioned frequency-routing phenomenon evident from the FRF curves and the field visualization at selected frequencies (9.780, 9.900, and 10.500 kHz marked by *D*–*F*, respectively).

It is worth noting that the devices reported in the literature for routing edge states are either bulky assemblies of TIs or TIs with movable domain walls. The intricacy makes them difficult for practical purposes. Our proposed anisotropic PTI with inherent directionality, on the other hand, might achieve the same functionality by simply switching the operating frequency in a single TI surrounded by ordinary insulators. The frequency ranges of the aforementioned three patterns can also be flexibly tuned within the band gap on demand by adjusting the distances between the attached pillars and their weights. These adjustments of parameters can also contribute to the design of right-angle-shaped routes like an L shape. But achieving more complex routes, such as a Z shape, may be restricted by the symmetry and anisotropy of the square lattice.

IV. CONCLUSIONS

We systematically investigate the edge states of anisotropic PTIs by theoretical, numerical, and experimental means. The two striking characteristics of the edge states generated by the purposely imposed anisotropy in the unit cells are well predicted by our discrete mechanical model. The directionality is attributed to the distinctive topological phases along the unit cell's two orthogonal directions. Frequency routing allows the edge states to be routed in three patterns as the operating frequency switches. These two characteristics can be realized in an elastic system, as exemplified by a pillared plate. The

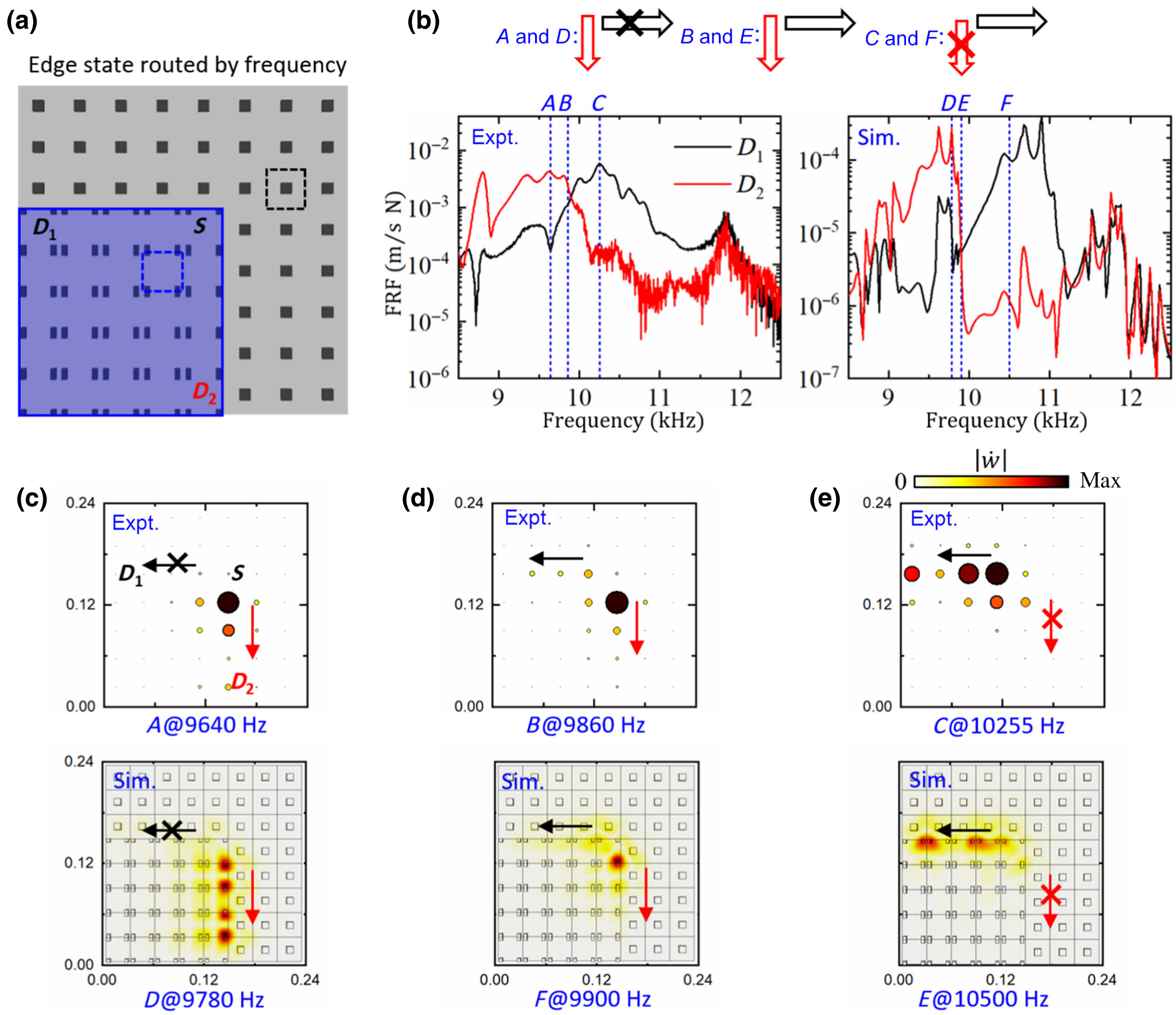

FIG. 7. Validation of the frequency routing of edge states. (a) Structure II is composed of isotropic (black dashed frame) and anisotropic (blue dashed frame) unit cells, with 2D polarization of (0, 0) and (π, π), respectively. S, D_1, and D_2 represent the excitation position and two detecting points, respectively. (b) Measured (left) and simulated (right) frequency-response functions of the structure at D_1 and D_2. (c)–(e) Measured (top) and simulated (bottom) fields of FRF corresponding to selected frequencies A–F in (b). Both color and radius of the circle reflect the amplitude of FRF at the scanned points.

proposed PTIs can overcome critical impediments present in conventional schemes, such as the stringent constraints on structural-dimension accuracy and the bulky attachment imposed by external controls, thus allowing one to route the edge state more easily. The proposed anisotropy in TIs provides a promising option for achieving tunability in elastic waveguiding devices. It may also inspire the reconfiguration of higher-order topological states.

APPENDIX A: FORMULA OF BAND STRUCTURES FOR THE ANISOTROPIC MECHANICAL LATTICE

The out-of-plane mode (flexural wave) in the thin elastic plate is considered. Therefore, the equivalent discrete model has just one degree of freedom for each mass. In an anisotropic unit cell located at (n_1, n_2), the displacements of the four masses, numbered from 1 to 4 in Fig. 1(a), are denoted as $u^i_{(n_1,n_2)}$, where $i = 1, 2, 3, 4$ denotes the mass index. To obtain the governing equation of the unit cell, Lagrange's equations (second kind) are employed [19]:

$$\frac{d}{dt}\left(\frac{\partial L}{\partial \dot{u}^i_{(n_1,n_2)}}\right) = \frac{\partial L}{\partial u^i_{(n_1,n_2)}}, \tag{A1}$$

in which Lagrangian $L = T - U$. The kinetic energy, T, and the potential energy, U, are obtained as

$$T = \frac{1}{2} m \sum_{i=1}^{4} \dot{u}^i_{(n_1,n_2)}{}^2, \tag{A2}$$

$$
\begin{aligned}
U = \frac{1}{2}\Big\{ & K_{\text{inter}}^{x}\left(u_{(n_1,n_2)}^{1} - u_{(n_1,n_2)}^{2}\right)^2 \\
& + K_{\text{inter}}^{y}\left(u_{(n_1,n_2)}^{2} - u_{(n_1,n_2)}^{3}\right)^2 \\
& + K_{\text{inter}}^{x}\left(u_{(n_1,n_2)}^{3} - u_{(n_1,n_2)}^{4}\right)^2 \\
& + K_{\text{inter}}^{y}\left(u_{(n_1,n_2)}^{4} - u_{(n_1,n_2)}^{1}\right)^2 \\
& + K_{\text{intra}}^{x}\left(u_{(n_1,n_2)}^{1} - u_{(n_1-1,n_2)}^{2}\right)^2 \\
& + K_{\text{intra}}^{y}\left(u_{(n_1,n_2)}^{1} - u_{(n_1,n_2-1)}^{4}\right)^2 \\
& + K_{\text{intra}}^{x}\left(u_{(n_1,n_2)}^{2} - u_{(n_1+1,n_2)}^{1}\right)^2 \\
& + K_{\text{intra}}^{y}\left(u_{(n_1,n_2)}^{2} - u_{(n_1,n_2-1)}^{3}\right)^2 \\
& + K_{\text{intra}}^{x}\left(u_{(n_1,n_2)}^{3} - u_{(n_1+1,n_2)}^{4}\right)^2 \\
& + K_{\text{intra}}^{y}\left(u_{(n_1,n_2)}^{3} - u_{(n_1,n_2+1)}^{2}\right)^2 \\
& + K_{\text{intra}}^{x}\left(u_{(n_1,n_2)}^{4} - u_{(n_1-1,n_2)}^{3}\right)^2 \\
& + K_{\text{intra}}^{y}\left(u_{(n_1,n_2)}^{4} - u_{(n_1,n_2+1)}^{1}\right)^2\Big\},
\end{aligned}
\tag{A3}
$$

in which the overdot notation represents the derivative with respect to time.

The Bloch wave solution of the infinite periodic lattice is

$$u_{(n_1,n_2)} = u_{(0,0)}e^{i[k(n_1a_1+n_2a_2)+\omega t]} \tag{A4}$$

where $u = (u_{(0,0)}^{1}, u_{(0,0)}^{2}, u_{(0,0)}^{3}, u_{(0,0)}^{4})$ represents the displacement of the four masses at location (0, 0), and $k = (k_x,\ k_y)$ is the Bloch wave vector. $a_1 = (1,\ 0)$ and $a_2 = (0,\ 1)$ are lattice vectors marked in Fig. 1(a), respectively.

Then we substitute Eqs. (A2)–(A4) into Eq. (A1), so the governing equation is derived as

$$\Omega^2\mathbf{M}u = \mathbf{K}u, \tag{A5}$$

in which the mass and stiffness matrices are written as

$$\mathbf{M} = \begin{bmatrix} m & 0 & 0 & 0 \\ 0 & m & 0 & 0 \\ 0 & 0 & m & 0 \\ 0 & 0 & 0 & m \end{bmatrix}$$

and

$$\mathbf{K} = \begin{bmatrix} k_{1,\,1} & k_{1,\,2} & k_{1,\,3} & k_{1,\,4} \\ k_{2,\,1} & k_{2,\,2} & k_{2,\,3} & k_{2,\,4} \\ k_{3,\,1} & k_{3,\,2} & k_{3,\,3} & k_{3,\,4} \\ k_{4,\,1} & k_{4,\,2} & k_{4,\,3} & k_{4,\,4} \end{bmatrix}_{4\times 4},$$

respectively. The matrix elements of the stiffness matrix are given below:

$$k_{i,\,i} = K_{\text{inter}}^{x} + K_{\text{intra}}^{x} + K_{\text{inter}}^{y} + K_{\text{intra}}^{y}\ (1 \le i \le 4,\ i \in \mathbf{Z}^{+}),$$

$$k_{1,\,2} = -K_{\text{inter}}^{x} - K_{\text{intra}}^{x}e^{-i\mathbf{q}a_1},\ k_{1,\,4} = -K_{\text{inter}}^{y} - K_{\text{intra}}^{y}e^{-i\mathbf{q}a_2},$$

$$k_{2,\,1} = -K_{\text{inter}}^{x} - K_{\text{intra}}^{x}e^{i\mathbf{q}a_1},\ k_{2,\,3} = -K_{\text{inter}}^{y} - K_{\text{intra}}^{y}e^{-i\mathbf{q}a_2},$$

$$k_{3,\,2} = -K_{\text{inter}}^{y} - K_{\text{intra}}^{y}e^{i\mathbf{q}a_2},\ k_{3,\,4} = -K_{\text{inter}}^{x} - K_{\text{intra}}^{x}e^{i\mathbf{q}a_1},$$

$$k_{4,\,1} = -K_{\text{inter}}^{y} - K_{\text{intra}}^{y}e^{i\mathbf{q}a_2},\ k_{4,3} = -K_{\text{inter}}^{x} - K_{\text{intra}}^{x}e^{-i\mathbf{q}a_1}.$$

The rest of the elements are zero. $\Omega = \omega\sqrt{4m/(K_{\text{inter}}^{x} + K_{\text{intra}}^{x} + K_{\text{inter}}^{y} + K_{\text{intra}}^{y})}$ denotes the dimensionless angular frequency. For further simplification, the transformation, $v = \mathbf{Q}u$, is used, where

$$\mathbf{Q} = \begin{bmatrix} \sqrt{m} & 0 & 0 & 0 \\ 0 & \sqrt{m} & 0 & 0 \\ 0 & 0 & \sqrt{m} & 0 \\ 0 & 0 & 0 & \sqrt{m} \end{bmatrix}.$$

Finally, Eq. (5) is converted into an eigenvalue problem as

$$\mathbf{H}v = \mathbf{Q}^{-1}\mathbf{K}\mathbf{Q}^{-1}v = \Omega^2 v, \tag{A6}$$

through which the band structure and the corresponding eigenstates can be numerically obtained by sweeping the Bloch wave vector, k, along the boundary of the first irreducible Brillouin zone, as depicted in Fig. 1(b).

APPENDIX B: SELECTED EIGENSTATES OF Figs. 1(c), 1(e), and 1(f)

The eigenstates at A, B, G, H, I and J marked in Figs. 1(c), 1(e), and 1(f) are given in Fig. 8.

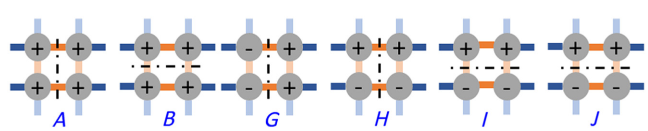

FIG. 8. Eigenstates at A, B, G, H, I, and J marked in Figs. 1(c), 1(e), and 1(f).

APPENDIX C: FORMULA OF BAND DISPERSION FOR RIBBON MECHANICAL LATTICE

To construct the ribbon mechanical lattice, we stack 1×8 anisotropic unit cells and 1×8 trivial isotropic unit cells. The top and bottom boundaries are set as Bloch periodical boundaries by using the one-dimensional Bloch wave solution:

$$u_{(n_1,n_2)} = u_{(n_1,n_2+1)} e^{i(a_2 k+\omega t)} \tag{C1}$$

The right and left ends are set as free boundaries. We set up the governing equations by applying Eq. (A1) (second kind). Such governing equations can also be further derived in the form of an eigenvalue problem:

$$\Omega^2 \mathbf{M} u = \mathbf{K} u. \tag{C2}$$

The mass matrix is diagonal and written as

$$\mathbf{M} = \begin{bmatrix} m & 0\cdots & 0 & \\ 0 & m & \cdots & 0 \\ \vdots & \vdots & \vdots & 0 \\ 0 & 0 & 0 & m \end{bmatrix}_{64\times 64}$$

.The stiffness matrix is

$$\mathbf{K} = \begin{bmatrix} k_{1,\,1} & k_{1,\,2} & \cdots & k_{1,\,64} \\ k_{2,\,1} & k_{2,\,2} & \cdots & k_{2,\,64} \\ \vdots & \vdots & \cdots & k_{3,\,64} \\ k_{64,\,1} & k_{64,\,2} & \cdots & k_{64,\,64} \end{bmatrix}_{64\times 64},$$

where the matrix elements $k_{i,\,j}$ are given in detail below.

For the diagonal elements,

$$k_{1,\,1} = k_{2,\,2} = 2K_{\text{inter}} + K_{\text{intra}}\; k_{63,\,63} = k_{64,\,64} = 2K_{\text{inter}} + K_{\text{intra}}.$$
$$k_{i,\,i} = 2(K_{\text{inter}} + K_{\text{intra}}), (3 \le i \le 30,\; i \in \mathbf{Z}^+).$$
$$k_{i,\,i} = K^x_{\text{inter}} + K^x_{\text{intra}} + K^y_{\text{inter}} + K^y_{\text{intra}}, (35 \le i \le 62,\; i \in \mathbf{Z}^+).$$
$$k_{31,\,31} = k_{32,\,32} = 2K_{\text{inter}} + K_{\text{intra}} + (K^x_{\text{intra}} + K_{\text{intra}})/2.$$
$$k_{33,\,33} = k_{34,\,34} = K^x_{\text{inter}} + K^y_{\text{intra}} + K^y_{\text{inter}} + (K^x_{\text{intra}} + K_{\text{intra}})/2.$$

For the nondiagonal elements,

$$k_{1,\,2} = -K_{\text{inter}} - K_{\text{intra}} e^{-ik_n a}\; k_{1,\,3} = k_{2,\,4} = -K_{\text{inter}}\; k_{2,\,1} = -K_{\text{inter}} - K_{\text{intra}} e^{ik_n a}.$$
$$k_{63,\,61} = k_{64,\,62} = -K^x_{\text{inter}} k_{63,\,64} = -K^y_{\text{inter}} - K^y_{\text{intra}} e^{-ik_n a}.$$
$$k_{64,\,63} = K^y_{\text{inter}} k^y_{\text{intra}} e^{ik_n a}.$$
$$k_{31,\,32} = -K_{\text{inter}} - K_{\text{intra}} e^{-ik_n a} k_{31,\,29} = -K_{\text{inter}} k_{31,\,33} = -(K_{\text{intra}} + K^x_{\text{intra}})/2.$$
$$k_{32,\,31} = -K_{\text{inter}} - K_{\text{intra}} e^{ik_n a} k_{32,\,30} = -K_{\text{inter}} k_{32,\,34} = -(K_{\text{intra}} + K^x_{\text{intra}})/2.$$
$$k_{33,\,34} = -K^y_{\text{inter}} - K^y_{\text{intra}} e^{-ik_n a} k_{33,\,35} = -K^x_{\text{inter}} k_{33,\,31} = -(K_{\text{intra}} + K^x_{\text{intra}})/2.$$
$$k_{34,\,33} = -K^y_{\text{inter}} - K^y_{\text{intra}} e^{ik_n a} k_{34,\,36} = -K^x_{\text{inter}} k_{34,\,32} = -(K_{\text{intra}} + K^x_{\text{intra}})/2.$$
$$k_{2i+1,\,2i+2} = -K_{\text{inter}} - K_{\text{intra}} e^{-ik_n a}, \quad (1 \le i \le 14,\; i \in \mathbf{Z}^+).$$
$$k_{2i,\,2i-1} = -K_{\text{inter}} - K_{\text{intra}} e^{ik_n a}, \quad (2 \le i \le 15,\; i \in \mathbf{Z}^+).$$

$$
\begin{aligned}
k_{2i+1,\,2i+2} &= -K^{y}_{\text{inter}} - K^{y}_{\text{intra}}e^{-ik_n a}, \quad (17 \le i \le 30,\ i \in \mathbf{Z}^+).\\
k_{2i,\,2i-1} &= -K^{y}_{\text{inter}} - K^{y}_{\text{intra}}e^{ik_n a}, \quad (18 \le i \le 31,\ i \in \mathbf{Z}^+).\\
k_{2i,\,2i-1} &= -K^{y}_{\text{inter}} - K^{y}_{\text{intra}}e^{ik_n a}, \quad (18 \le i \le 31,\ i \in \mathbf{Z}^+).\\
k_{4i-1,4i-3} &= -K_{\text{inter}},\ k_{4i-1,4i+1} = -K_{\text{intra}}, \quad (1 \le i \le 7,\ i \in \mathbf{Z}^+).\\
k_{4i,4i-2} &= -K_{\text{inter}},\ k_{4i,4i+2} = -K_{\text{intra}}, \quad (1 \le i \le 7,\ i \in \mathbf{Z}^+).\\
k_{4i+1,4i-1} &= -K_{\text{intra}},\ k_{4i+1,4i+3} = -K_{\text{inter}}, \quad (1 \le i \le 7,\ i \in \mathbf{Z}^+).\\
k_{4i+2,4i} &= -K_{\text{intra}},\ k_{4i,4i+4} = -K_{\text{inter}}, \quad (1 \le i \le 7,\ i \in \mathbf{Z}^+).\\
k_{4i-1,4i-3} &= -K^{x}_{\text{inter}},\ k_{4i-1,4i+1} = -K^{x}_{\text{intra}}, \quad (2 \le i \le 15,\ i \in \mathbf{Z}^+).\\
k_{4i,4i-2} &= -K^{x}_{\text{inter}},\ k_{4i,4i+2} = -K^{x}_{\text{intra}}, \quad (9 \le i \le 15,\ i \in \mathbf{Z}^+).\\
k_{4i+1,4i-1} &= -K^{x}_{\text{intra}},\ k_{4i+1,4i+3} = -K^{x}_{\text{inter}}, \quad (9 \le i \le 15,\ i \in \mathbf{Z}^+).\\
k_{4i+2,4i} &= -K^{x}_{\text{intra}},\ k_{4i,4i+4} = -K^{x}_{\text{inter}}, \quad (9 \le i \le 15,\ i \in \mathbf{Z}^+).
\end{aligned}
$$

The rest of the elements are zero. After a similar transformation to that in Appendix A and sweeping the Bloch wave vector k within $[0,\ \pi/a]$, the band dispersion can be obtained.

APPENDIX D: SELECTED EIGENSTATES OF Figs. 3(b) and 3(c)

Eigenstates at C, D, G, and H marked in Figs. 3(b) and 3(c) are given in Fig. 9.

APPENDIX E: EXPERIMENTAL SETUP

Figures 10(a) and 10(b) present structures I and II of the samples used in experiments, respectively. The samples are made of bare aluminum substrate plate, on which steel pillars are glued using acrylic adhesive. To suppress the inherent structure resonance and avoid reflections from the plate boundaries, a high-stickiness bonding agent, Blu Tack, is attached to the borders. The substrate plate is lengthened along the propagating direction to reduce reflections. Figures 10(c) and 10(d) show the experimental arrangement. The samples are suspended on thin strings. A force transducer is glued at the plate side with pillars. The bare sides of the samples are scanned by a Polytec scanning laser vibrometer.

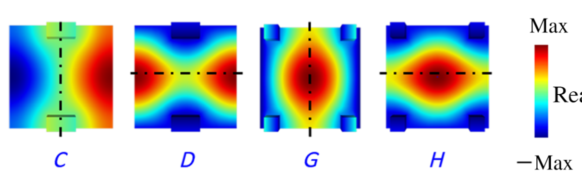

FIG. 9. Eigenstates at C, D, G, and H marked in Figs. 3(b) and 3(c). Rainbow-color bar represents the real part of out-of-plane displacement real(w).

The schematic of the signal path is depicted in Fig. 10(e). The built-in generator sends out a periodic up-chirp signal with frequencies ranging from 8 to 13 kHz, which is amplified to drive the electromechanical shaker and excite the desired edge states. Meanwhile, a force transducer is mounted between the shaker and the plate to provide the reference excitation-force signal to the computer. The complex FRF can be derived by normalizing the scanning velocity with respect to the measured force signal and conducting the fast Fourier transform. It reflects the complex velocity at specific locations of the samples after minimizing impacts from the shaker itself.

APPENDIX F: SIMULATION DETAILS

All simulations are performed with COMSOL Multiphysics (v5.6). The band structures and eigenmodes are calculated by solving eigenvalue problems. The unit cell's top, bottom, right, and left surfaces are imposed as Floquet boundaries, while the rest is set as free. Only the right and left surfaces of the ribbon structure are imposed Floquet boundaries. To reduce boundary reflection, the FRFs are solved using a frequency-domain solver with the top, bottom, right, and left surfaces enforced as low-reflecting boundary conditions. A unitary point force in the out-of-plane direction is loaded to act as the excitation source.

ACKNOWLEDGMENTS

This work is supported by the Fundamental Research Funds for the Central Universities (Grant No. 221202 20237), the National Natural Science Foundation of China (Grant No. 1210020421), and the Research Grants Council of Hong Kong SAR (Grant No. AoE/P-502/20).

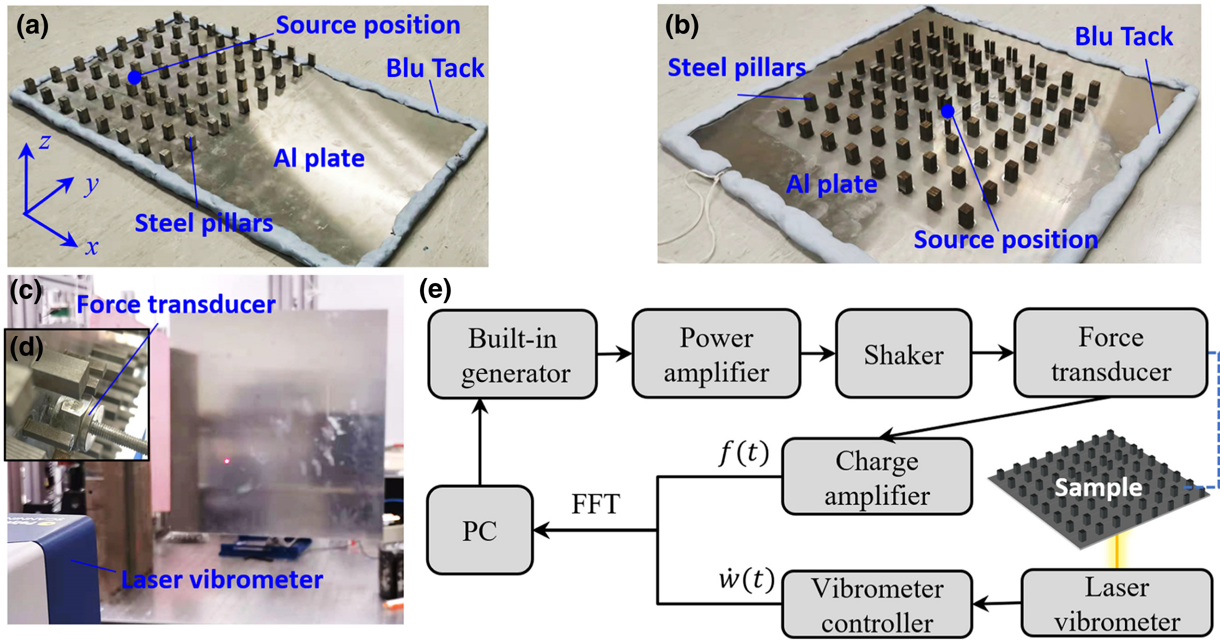

FIG. 10. Experimental setup. Fabricated samples for structures (a) I and (b) II. (c) Samples are hung from strings and scanned by a laser vibrometer. (d) Force transducer is glued to the back of the samples. (e) Signal path for measurements.

[1] Z. Liu, X. Zhang, Y. Mao, Y. Y. Zhu, Z. Yang, C. T. Chan, and P. Sheng, Locally resonant sonic materials, Science **289**, 1734 (2000).

[2] L. Cao, Z. Yang, Y. Xu, S.-W. Fan, Y. Zhu, Z. Chen, Y. Li, and B. Assouar, Flexural wave absorption by lossy gradient elastic metasurface, J. Mech. Phys. Solids **143**, 104052 (2020).

[3] C. R. Farrar and K. Worden, An introduction to structural health monitoring, Philos. Trans. R. Soc., A **365**, 303 (2007).

[4] S. Shan, Z. Liu, L. Cheng, and Y. Pan, Metamaterial-enhanced coda wave interferometry with customized artificial frequency-space boundaries for the detection of weak structural damage, Mech. Syst. Signal Process. **174**, 109131 (2022).

[5] T. Worlikar, M. Zhang, A. Ganguly, T. L. Hall, J. Shi, L. Zhao, F. T. Lee, M. Mendiratta-Lala, C. S. Cho, and Z. Xu, Impact of histotripsy on development of intrahepatic metastases in a rodent liver tumor model, Cancers **14**, 1612 (2022).

[6] Y. Chen, Q. Zhang, Y. Zhang, B. Xia, X. Liu, X. Zhou, C. Chen, and G. Hu, Research progress of elastic topological materials, Adv. Mech. **51**, 189 (2021).

[7] X. Li, S. Yu, H. Liu, M. Lu, and Y. Chen, Topological mechanical metamaterials: A brief review, Curr. Opin. Solid State Mater. Sci. **24**, 100853 (2020).

[8] H. Huang, J. Chen, and S. Huo, Recent advances in topological elastic metamaterials, J. Phys.: Condens. Matter **33**, 503002 (2021).

[9] P. Wang, L. Lu, and K. Bertoldi, Topological Phononic Crystals with One-Way Elastic Edge Waves, Phys. Rev. Lett. **115**, 104302 (2015).

[10] S. Yu, C. He, Z. Wang, F. Liu, X. Sun, Z. Li, H. Lu, M. Lu, X. Liu, and Y. Chen, Elastic pseudospin transport for integratable topological phononic circuits, Nat. Commun. **9**, 3072 (2018).

[11] Y.-T. Wang, P.-G. Luan, and S. Zhang, Coriolis force induced topological order for classical mechanical vibrations, New J. Phys. **17**, 073031 (2015).

[12] Y. Zhao, X. Zhou, and G. Huang, Non-reciprocal Rayleigh waves in elastic gyroscopic medium, J. Mech. Phys. Solids **143**, 104065 (2020).

[13] S. H. Mousavi, A. B. Khanikaev, and Z. Wang, Topologically protected elastic waves in phononic metamaterials, Nat. Commun. **6**, 8682 (2015).

[14] M. Miniaci, R. K. Pal, B. Morvan, and M. Ruzzene, Experimental Observation of Topologically Protected Helical Edge Modes in Patterned Elastic Plates, Phys. Rev. X **8**, 031074 (2018).

[15] S. An, T. Liu, H. Fan, H. Gao, Z. Gu, S. Liang, S. Huang, Y. Zheng, Y. Chen, L. Cheng, and J. Zhu, Second-order elastic topological insulator with valley-selective corner states, Int. J. Mech. Sci. **224**, 107337 (2022).

[16] H. Chen, H. Nassar, and G. L. Huang, A study of topological effects in 1D and 2D mechanical lattices, J. Mech. Phys. Solids **117**, 22 (2018).

[17] Q. Wu, H. Chen, X. Li, and G. Huang, In-Plane Second-Order Topologically Protected States in Elastic Kagome Lattices, Phys. Rev. Lett. **14**, 014084 (2020).

[18] Y. Yang, H. Jiang, and Z. H. Hang, Topological valley transport in two-dimensional honeycomb photonic crystals, Sci. Rep. **8**, 1588 (2018).

[19] R. K. Pal and M. Ruzzene, Edge waves in plates with resonators: an elastic analogue of the quantum valley Hall effect, New J. Phys. **19**, 025001 (2017).

[20] Q. Zhang, Y. Chen, K. Zhang, and G. Hu, Programmable elastic valley Hall insulator with tunable interface propagation routes, Extreme Mech. Lett. **28**, 76 (2019).

[21] G.-H. Li, T.-X. Ma, Y.-Z. Wang, and Y.-S. Wang, Active control on topological immunity of elastic wave metamaterials, Sci. Rep. **10**, 9376 (2020).

[22] M. Yan, J. Lu, F. Li, W. Deng, X. Huang, J. Ma, and Z. Liu, On-chip valley topological materials for elastic wave manipulation, Nat. Mater. **17**, 993 (2018).

[23] Y. Chen, F. Meng, Y. Kivshar, B. Jia, and X. Huang, Inverse design of higher-order photonic topological insulators, Phys. Rev. Res. **2**, 023115 (2020).

[24] G. Wei, Z. Liu, Y. Liu, D. Zhang, and J. Xiao, Frequency selective topological edge wave routing in meta-structures made of cylinders, Opt. Lett. **45**, 5608 (2020).

[25] W. Yuan, J. Zhao, Y. Long, J. Ren, and Z. Zhong, Multibranch valley-chiral edge states of antisymmetric plate wave in phononic crystal plates with double-sided symmetric pillars, Int. J. Mech. Sci. **197**, 106347 (2021).

[26] G.-C. Wei, Z.-Z. Liu, D.-S. Zhang, and J.-J. Xiao, Frequency dependent wave routing based on dual-band valley-Hall topological photonic crystal, New J. Phys. **23**, 023029 (2021).

[27] Z. Huang, J. Wu, C. Wang, S. Yang, and F. Ma, Resonant-Scattering Hybrid Device for Multiband Acoustic Topology Valley Transmission, Phys. Rev. Lett. **104**, 094110 (2021).

[28] G. Ma, C. Fu, G. Wang, P. del Hougne, J. Christensen, Y. Lai, and P. Sheng, Polarization bandgaps and fluid-like elasticity in fully solid elastic metamaterials, Nat. Commun. **7**, 13536 (2016).

[29] J. Zhu, J. Christensen, J. Jung, L. Martin-Moreno, X. Yin, L. Fok, X. Zhang, and F. J. Garcia-Vidal, A holey-structured metamaterial for acoustic deep-subwavelength imaging, Nat. Phys. **7**, 52 (2011).

[30] L. Wu, M. Oudich, W. Cao, H. Jiang, C. Zhang, J. Ke, J. Yang, Y. Deng, Q. Cheng, T. Cui, and Y. Jing, Routing Acoustic Waves via a Metamaterial with Extreme Anisotropy, Phys. Rev. Appl. **12**, 044011 (2019).

[31] J. Christensen and F. J. G. de Abajo, Anisotropic Metamaterials for Full Control of Acoustic Waves, Phys. Rev. Lett. **108**, 124301 (2012).

[32] J. M. Kweun, H. J. Lee, J. H. Oh, H. M. Seung, and Y. Y. Kim, Transmodal Fabry-Pérot Resonance: Theory and Realization with Elastic Metamaterials, Phys. Rev. Lett. **118**, 205901 (2017).

[33] X.-D. Chen, W.-M. Deng, F.-L. Shi, F.-L. Zhao, M. Chen, and J.-W. Dong, Direct Observation of Corner States in Second-Order Topological Photonic Crystal Slabs, Phys. Rev. Lett. **122**, 233902 (2019).

[34] J. Lu, K. G. Wirth, W. Gao, A. Heßler, B. Sain, T. Taubner, and T. Zentgraf, Observing 0D subwavelength-localized modes at $\sim$100 THz protected by weak topology, Sci. Adv. **7**, eabl3903 (2021).

[35] Z.-G. Chen, J. Zhao, J. Mei, and Y. Wu, Acoustic frequency filter based on anisotropic topological phononic crystals, Sci. Rep. **7**, 15005 (2017).

[36] Y. Ding, Y. Peng, Y. Zhu, X. Fan, J. Yang, B. Liang, X. Zhu, X. Wan, and J. Cheng, Experimental Demonstration of Acoustic Chern Insulators, Phys. Rev. Lett. **122**, 014302 (2019).

[37] Z. Zhang, H. Long, C. Liu, C. Shao, Y. Cheng, X. Liu, and J. Christensen, Deep-subwavelength holey acoustic second-order topological insulators, Adv. Mater. **31**, 1904682 (2019).

[38] Y. Chen, Z. Lan, and J. Zhu, Second-order topological phases in $C4v$-symmetric photonic crystals beyond the two-dimensional Su-Schrieffer–Heeger model, Nanophotonics **11**, 1345 (2022).